

Thermomechanical Simulation of Heat-Affected Zones in Nickel-Free High Nitrogen Stainless Steel: Microstructural Evolution and Mechanical Property Studies

Dhanasekar Ramalingam^{a*} , Balusamy Veerappagounder^b, Sivasankari Rangaswamy^a 

^aPSG College of Technology, Department of Metallurgical Engineering, Coimbatore, 641 004, Tamilnadu, India.

^bKongu Engineering College, Department of Mechanical Engineering, Erode, 638 060, Tamilnadu, India.

Received: September 07, 2022; Revised: January 19, 2023; Accepted: February 1, 2023

Three different Heat Affected Zones (HAZ) in hot rolled Nickel Free High Nitrogen Stainless Steels (NFHNSS) based on three different peak temperatures were physically simulated using Gleeble Simulator to investigate microstructural evolution and structure-property correlation. Optical microscopy revealed that the austenite grains are recrystallized in the simulated heat affected zone in the peak temperature range of 750 °C to 1050 °C. Extent of recrystallization of grains and nucleation of precipitates varied with peak temperatures. TEM characterization showed the presence of Cr₂N precipitate having an average particle size in the range of 300 nm to 395 nm in the simulated HAZ were confirmed by Selected Area Electron Diffraction (SAED) analysis. Precipitation kinetics of Cr₂N were simulated using Thermo-Calc were found to correlate well with experimental values. Mechanical properties of specimens taken from three different HAZ were evaluated for tensile strength and hardness. Variation in strength of the different specimens has been discussed using various strengthening models. Fractography analysis was also carried out to understand the effect of peak temperature on fracture behaviour. Transition in fracture patterns in NFHNSS from ductile to mixed mode was observed for different specimens.

Keywords: Nickel free High Nitrogen Stainless Steel (NFHNSS), Thermomechanical simulation, TEM, Chromium Nitride, HAZ.

1. Introduction

Nickel-Free High Nitrogen Stainless Steel (NFHNSS) containing 0.4% N are being considered for applications in defence, power plant and aerospace applications. In particular, ballistic tank shields fabricated from High Nitrogen Stainless Steel (HNSS) can be a viable replacement for conventional armour steels. HNSS possess excellent yield strength (>1000 MPa) along with good toughness, ductility and pitting resistance^{1,2}. Nickel is replaced by nitrogen in austenitic stainless steel for both superior mechanical properties as well as cost benefits. In NFHNSS, addition of manganese aids in reducing the stacking fault energy which facilitates increased solubility of nitrogen in steel. However, manganese has a detrimental effect on localized corrosion resistance and can be compensated by increasing the nitrogen content of the steel³.

Welding of NFHNSS is an important area of research since a quality weld with adequate mechanical properties along with good corrosion resistance is required for many applications. Nitrogen loss in the weld zone, nitrogen induced porosity, solidification cracking, liquation cracking, δ -ferrite formation during different thermal cycling as well as precipitation of carbides and nitrides in the Heat Affected Zone (HAZ) are significant metallurgical issues involved in the welding of

NFHNSS⁴⁻⁶. Proper selection of welding process as well as welding parameters, choice of electrodes and careful evaluation of the solidification behaviour helps in achieving a good weldment property. Mohammed et al.⁷ reported the influence of microstructure on HAZ properties in NFHNSS formed under various thermal cycling. Mukherjee and Pal⁸ reported that the heat input played a major role in the formation of M₂₃C₆ and M₂N precipitates along the grain boundaries during high-temperature thermal cycling. Rod like Cr₂N precipitates were found in simulated HAZ specimens of weld thermal cycle with heat input of 5 kJ/cm on duplex steel exposed at 700 °C was observed by Chen and Yang⁹. Wang et al.¹⁰ reported that increasing the heat input from 8 kJ/cm to 36 kJ/cm with different t_{8/5} values increases the volume fraction of precipitates from 10.07% to 16.85% respectively. Similarly, with the increase of cooling rate, the fraction of Cr₂N precipitates decreases from 13.8% to 2.9% in HNSS is observed by Li et al.¹¹. Nitrogen enhances the properties when it is retained in solid solution, but nitrides were formed at higher peak temperatures has a detrimental effect on ductility and mechanical strength. Precipitation kinetics of Cr₂N were reported in Fe–20Mn–12Cr–0.24C–0.32N alloy that precipitation of Cr₂N is favoured at 900 °C, as the driving force is higher at this temperature¹². Krishna Kumar et al.¹³ reported the kinetics of nitride precipitation at 700°C to 900°C aging temperatures using CALPHAD

*e-mail: dhana130909@gmail.com

simulation. Simulations studies were also carried out by Lang et al.¹⁴ to investigate the effect of various alloying elements (C, Cr, Mn and Ni) on nitrogen solubility at 1000°C to 1200°C and found that stable austenite phase were simulated within a given range of alloying elements using Thermo-Calc. Behjati et al.¹⁵ investigated the effect of nitrogen content on grain refinement and strengthening mechanisms in Ni-free 18Cr-12Mn austenitic stainless steel. Various strengthening models influencing the mechanical strength of Fe-13Mn-1.3C austenitic steels under different deformation conditions have been reported by Maier and Astafurova¹⁶. Similarly, quantitative models have been developed by Farooq¹⁷ for predicting the strength contribution in austenitic stainless steels at elevated temperatures.

Limited literature were reported on simulation studies on precipitation kinetics and the effect of peak temperature and cooling rate on the microstructural and mechanical properties of NFHNSS weldments. Hence, the main objective of the present study was to simulate three different HAZ's with different peak temperature using Gleeble thermo-mechanical simulator and correlate the evolved microstructure with the mechanical properties of NFHNSS. Further, Precipitation kinetics of Cr₂N particles in the various HAZ zones of NFHNSS have also been investigated using Thermo-Calc.

2. Materials and Methods

Nickel-Free High Nitrogen Stainless Steel (NFHNSS) having a chemical composition of 0.06C, 18Cr, 22Mn and 0.55N (wt%) was chosen for thermo-mechanical simulation. Welding parameters for thermo-mechanical simulation of heat affected zone were obtained by conducting SMAW trial experiments on 10 mm thick hot rolled NFHNSS plates. From the trial study data, three different HAZ were identified from the weld centre-line towards base material based on different microstructural morphology and were designated as HAZ-1 HAZ-2 and HAZ-3 respectively (Figure 1). Three specimens having dimension of 86 mm (length) x 10 mm (width) x 10 mm (thickness) were used in the HAZ simulation for three different zones. Physical simulation of the samples was carried out using Gleeble-3500 under argon atmosphere with welding heat input of 6 kJ/cm and welding speed of 4 mm/s. 3D-Rykalin mathematical model was used for determining the thermal cycle curve of NFHNSS specimens¹⁸⁻²⁰. Simulated specimens were subsequently investigated for microstructural characterization and mechanical property evaluation.

As received (hot rolled) and HAZ simulated NFHNSS specimens were polished and electrolytically etched using an

aqueous solution containing a mixture of 20 g oxalic acid and 200 ml distilled water. A Leica (DMi8C model) light polarized microscope was used to characterize the microstructure of the specimens. Grain size measurement was carried out using a Leica grain size analyzer as per ASTM E-112 standard²¹. An average of 10 readings was taken as the average grain size with an accuracy level of 0.097 microns/pixels. Specimens for Transmission Electron Microscope (TEM) investigations were prepared by mechanical polishing and further thinned down by ion milling. TEM analysis, using both imaging and Selected Area Diffraction modes were carried out on a JEOL-JEM-2100 instrument at an operating voltage of 200 kV. Volume fraction of secondary phases and dislocation density were estimated from TEM micrographs using Image-J software. Lattice points with zone axis of the primary phase and secondary phases in NFHNSS specimens were also investigated by SAED imaging.

Simulation of phase diagram of NFHNSS based on CALPHAD approach was carried out using Thermo-Calc software (TCFE8 database). Temperature-time data obtained from physical simulation of three different HAZ specimens were used for simulating the precipitation kinetics based on Langer-Schwartz theory and Kampmann-Wagner numerical approach using TC-PRISMA (Thermo-Calc Precipitation) module. Nucleation rate ($m^{-3}s^{-1}$), mean particle size (nm), driving force for precipitation and volume fraction of precipitates were determined using TC-PRISMA mobility database under arbitrarily selected non-equilibrium conditions based on experimental thermal profiles. These simulated data were used to determine the kinetics of particle coarsening of Cr₂N precipitates²². Room temperature tensile testing of the simulated specimens was carried out using an INSTRON micro-tensile testing machine at a constant strain rate of 0.001 s⁻¹. Tensile specimens having a gauge length of 16 mm were prepared by Electric Discharge Machining (EDM) and an average of three measurements was taken as the tensile strength. Fractography of tensile tested specimen was carried out using JEOL Scanning Electron Microscope. Subsequently, hardness measurements were done using a Zwick Vickers micro hardness tester with a 10 kgf load for a dwell time of 15 seconds and an average of five trials were taken as the hardness.

3. Results and Discussion

3.1. Microstructural characterization

Figure 2 shows the optical micrographs of base metal and simulated HAZ of NFHNSS specimens. Hot rolled

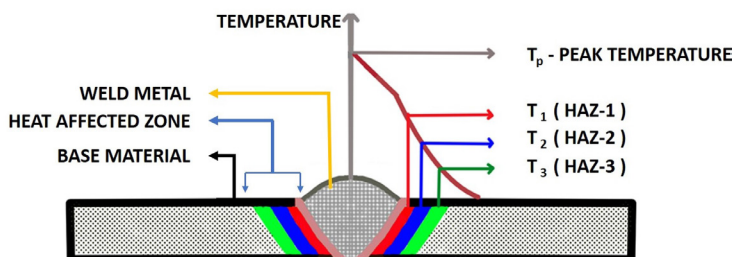


Figure 1. Schematic representation of heat affected zones during welding.

NFHSS specimen (Figure 2a) showed deformed austenite grains containing annealing twins with an average grain size of about $40 \pm 2 \mu\text{m}$. Few grains showed abnormal growth due to strain-induced grain boundary migration during hot rolling of NFHSS. Similar observations have been reported by Rios et.al during their investigations on austenitic stainless steels²³.

Microstructure of the HAZ-1 specimen (Figure 2b) showed predominantly equiaxed austenite grains, with an average grain size of about $33 \pm 1.65 \mu\text{m}$. The formation of such grains is favoured by static recrystallization owing to a reduction in the stored energy of deformed grains and twins during thermal cycling. The degree of recrystallization depends on local differences in dislocation density which provides the driving force for nucleation of grain at the grain boundaries as reported by Sellars and Whiteman²⁴. Grain coarsening was facilitated by high peak temperatures with slow cooling rate. For HAZ-2 specimen, microstructure comprised of fine recrystallized austenite grains along with a few deformed grains having an average grain size of $19 \pm 0.95 \mu\text{m}$ (Figure 2c). This can be associated with a relatively low peak temperature and shorter time for recrystallization. In the case of HAZ-3 specimen, optical micrograph (Figure 2d) showed bimodal grain morphology of partially recrystallized austenite grains and deformed grains having an average grain size of $26 \mu\text{m} \pm 0.5 \mu\text{m}$ is due to lower peak temperature during the thermal cycle. Primary reason for the partial recrystallization and bimodal grain morphology is due to lower peak temperature and some of the deformed grains having higher stored energy recrystallize effectively compared to the grains with relatively lower stored energy. Misra have reported a similar result during his studies on hot rolled micro alloyed steels²⁵.

The TEM micrograph of hot rolled NFHSS specimen (Figure 3a) exhibited the presence of dense dislocation and deformation twins in the austenite matrix. The dislocation

density for the specimen was calculated using intercept method ($\rho = 2nM/Lt$) by drawing a circle with circumference (L) 200 mm over the micrograph of 100000X magnification (M) using Image-J software. The numbers of dislocation intercept (n) were counted as 70 with foil thickness (t) of 120 nm. The dislocation density of hot rolled specimen was $5.87 \times 10^{14} \text{ m}^{-2}$ ²⁶. Austenite phase was identified in the SAED pattern with a zone axis of [0 1 1]. TEM analysis of base metal show absence of Cr_2N precipitate. Figure 3b shows the bright field image of the HAZ-1 specimen. It can be observed that the formation of Cr_2N precipitates occurred at the grain boundaries of the austenitic matrix. It has been reported that higher nitrogen levels in the alloy reduced the driving force for nucleation and growth of M_{23}C_6 and sigma phase compared to Cr_2N precipitates in NFHSS²⁷.

Figure 4 shows the peak temperature of physically simulated NFHSS specimen. The peak temperature and cooling rate of HAZ-1 specimen nearer to the fusion zone are 1052°C and 20°C/s respectively. Since HAZ-1 exhibits peak temperature above 925°C and cooling rate is 20°C/s , nucleation of Cr_2N is favoured at the grain boundaries during thermal cycling. This can be justifiable since nitrogen has more affinity towards chromium than carbon²⁸. Woo and Kikuchi² also reported that Cr_2N precipitates at a very slow cooling rate below 20°C/s in the HAZ containing 0.75 wt. %N in HNSS since there is sufficient time for precipitation during cooling. In the present study, it can be observed that the Cr_2N precipitate was also surrounded by a few dislocation tangles. Thus, it can be concluded that stored energy of dislocation tangles provides a sufficient driving force for the formation of Cr_2N precipitates. The dislocation density was found to reduce to $2.2 \times 10^{14} \text{ m}^{-2}$ compared to that of the hot rolled specimen. Further, the morphology of Cr_2N precipitates was found to be globular in nature (395 nm), facilitated by high peak temperature. The presence of Cr_2N precipitates was confirmed by the indexed SAED pattern

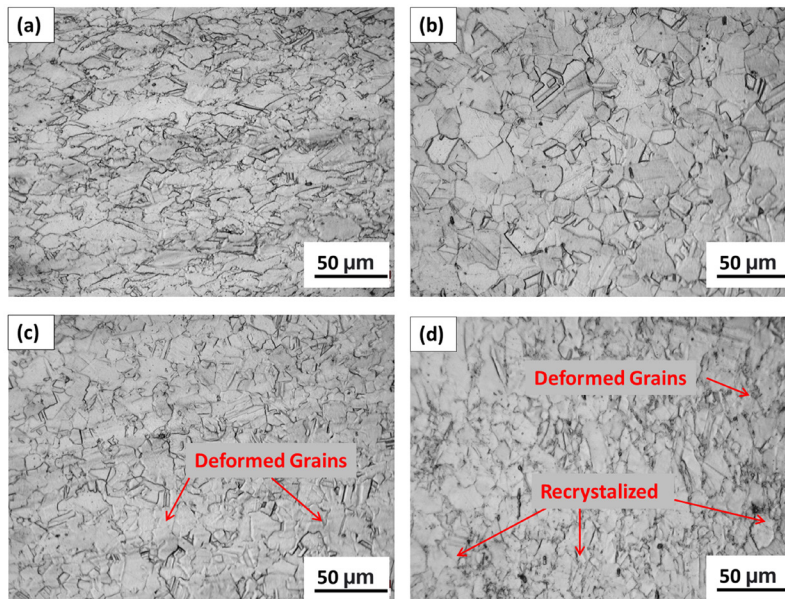


Figure 2. Microstructure of Heat Affected Zone of NFHSS (a) Hot rolled, (b) HAZ -1, (c) HAZ - 2 and (d) HAZ - 3 specimen.

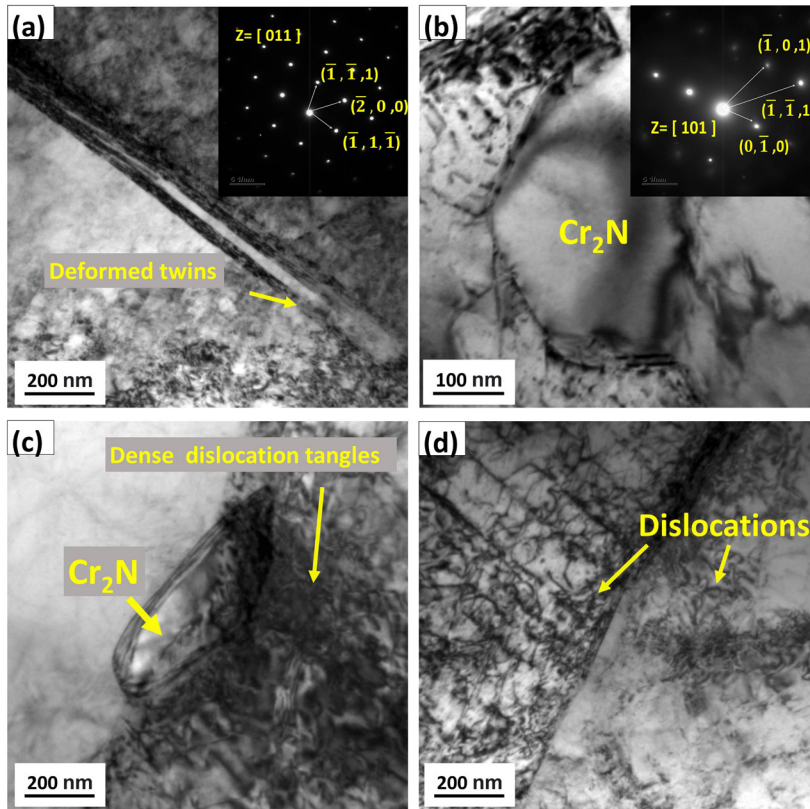


Figure 3. TEM micrographs of NFHNSS samples (a) Hot rolled specimen with SAED indexing, (b) HAZ -1, (c) HAZ – 2 and (d) HAZ – 3 specimen.

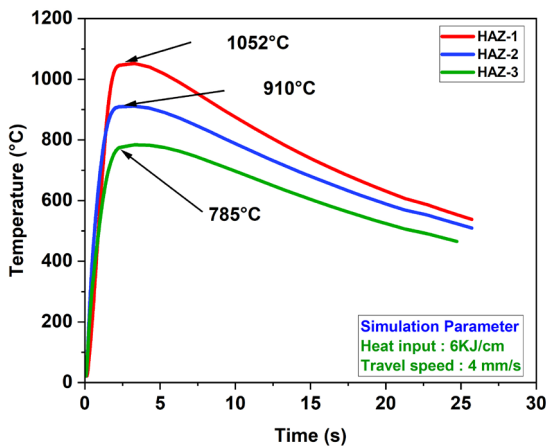


Figure 4. Physically simulated HAZ thermal cycle using Gleeble simulator.

obtained from the $[1\ 0\ 1]$ zone axis representing a HCP lattice with $a = 0.2748$ nm and $c = 0.4438$ nm respectively. This data closely matches with the standard diffraction pattern of Cr_2N precipitate²⁹.

Similarly, the peak temperature and cooling rate of the HAZ-2 specimen was found to be 910°C and 17°C/s respectively also favoured the formation of Cr_2N precipitates. As seen from Figure 3c, the HAZ-2 specimen showed the

presence of catenary type Cr_2N precipitate with a particle size of 260 nm at the grain boundary. It was also found that a dislocation density ($2.93 \times 10^{14}\ \text{m}^{-2}$) in the HAZ-2 specimen was relatively higher compared to that of the HAZ-1 specimen due to a low peak temperature. Significant difference in the morphology of Cr_2N precipitate between the HAZ-1 and HAZ-2 specimen arises due to variation in surface energy of precipitates imposed by the different peak temperature and cooling rate during thermal cycle.

HAZ-3 specimen (Figure 3d) showed the presence of dense dislocation tangles with the dislocation density of $5.13 \times 10^{14}\ \text{m}^{-2}$ and very few Cr_2N precipitates owing to low peak temperature. Peak temperature of the HAZ-3 specimen was 785°C and cooling rate is 16°C/s . At this temperature, the extent of formation of Cr_2N precipitates was found to reduce significantly due to low driving force. It can be also inferred that the driving force for nucleation of Cr_2N precipitates tends to vary with cooling rate and exposure time at higher temperatures³⁰. Thus, precipitate morphology and nucleation time for the formation of Cr_2N precipitates is determined by cooling rate and reaction kinetics between nitrogen with chromium.

3.2. Precipitation kinetics of Cr_2N

Simulated property diagram (Figure 5) showed that formation of delta ferrite begins at a temperature of 1375°C and subsequently gets transformed to an austenite phase at a temperature of 1185°C during solidification. A complete

austenitic structure exists between 1185 °C and 925 °C. The critical temperature of different phases, namely Cr₂N, sigma and M₂₃C₆ precipitates formed were found to be 925 °C, 831 °C and 822 °C, respectively. In addition, the maximum phase fraction of sigma, Cr₂N and M₂₃C₆ precipitates were found to be 0.42, 0.008 and 0.002 moles respectively. Gavriljuk and Berns²⁸ reported that Cr₂N could be the predominant precipitate since higher nitrogen content suppresses the formation of sigma and M₂₃C₆ precipitates in NFHNSS.

Nucleation rate of Cr₂N precipitates (Figure 6a) simulated using TC-PRISMA for the three heat affected zones exhibiting different peak temperatures. Maximum nucleation rates for the formation of Cr₂N precipitates in HAZ-1, HAZ-2 and HAZ-3 were 1.256 x 10²⁴ m⁻³s⁻¹, 7.75 x

10²³ m⁻³s⁻¹ and 2.73 x 10²³ m⁻³s⁻¹, respectively. The nucleation rate of Cr₂N precipitate in HAZ-1 specimen was found to be higher than that of HAZ-2 specimen owing to the higher peak temperature. Lowest nucleation rate was observed for the HAZ-3 specimen due to lowest peak temperature. Such variation in nucleation rate greatly influences the volume fraction of the precipitates, and this result is in correlation to TEM results of HAZ specimen.

Figure 6b shows normalized driving force for the nucleation of Cr₂N precipitates for the three heat affected zones. Driving force for the formation of Cr₂N precipitate in the HAZ specimen was nearly the same and changed gradually with cooling rate. Conversely, the driving force for HAZ-1 and HAZ-2 confirms the nucleation of stable Cr₂N precipitates. The driving force remained in a narrow range for HAZ-3 as the nucleation of precipitates was lower due to a low peak temperature. Figure 6c shows the maximum volume fraction of Cr₂N precipitate for the three heat affected zones. The maximum volume fraction remains 0.008 wt% for HAZ-1 and HAZ-2 specimens. HAZ-3 specimen required a longer incubation period to achieve a precipitate volume fraction of 0.0046 wt % compared to HAZ-1 and HAZ-2 specimens. After the incubation period, the volume fraction of the Cr₂N precipitate increased exponentially with time. Particle size of Cr₂N precipitate (Figure 6d) as a function of time for the three different HAZ specimens showed that the maximum precipitate size for HAZ-1, HAZ-2 and HAZ-3 specimens were found in the range of 3 nm. However, TEM studies revealed that the particle sizes of Cr₂N precipitate in HAZ were in the range of 395 nm to 260 nm. Such difference in particle size of Cr₂N precipitate arises because of varying cooling conditions imposed by the simulated thermal cycle.

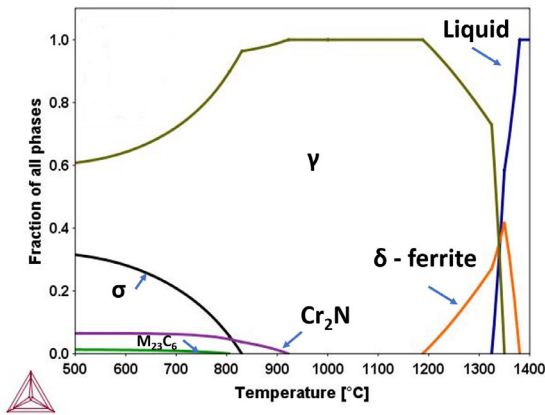


Figure 5. Phase diagram of NFHNSS alloy (18Cr-22Mn-0.55N).

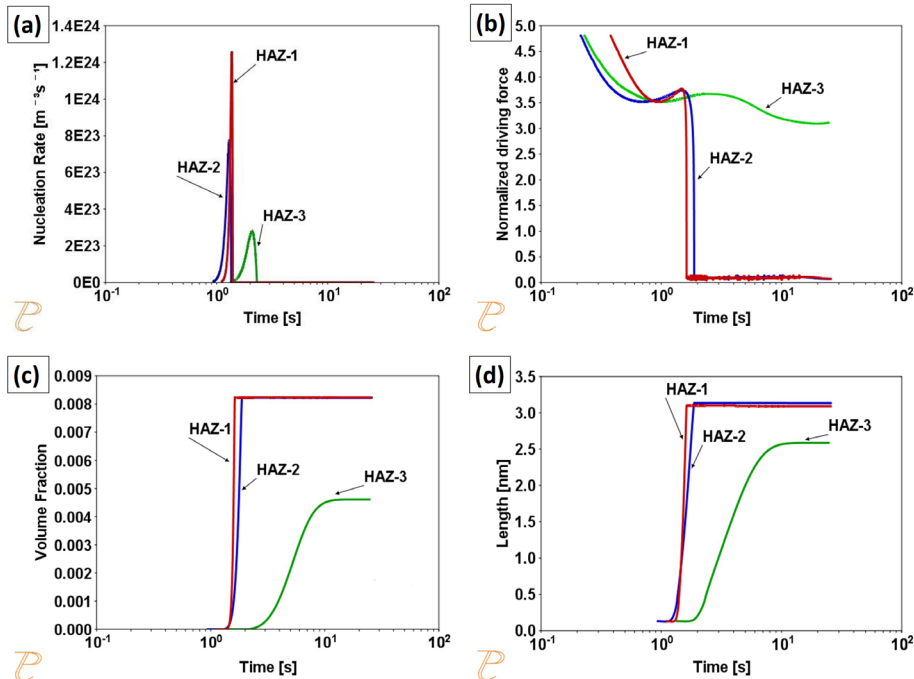


Figure 6. Precipitation kinetics of Cr₂N in heat affected zones simulated using TC-PRISMA (a) Nucleation rate, (b) Normalized driving force, (c) Volume fraction of Cr₂N precipitate and (d) Mean size of precipitate.

3.3. Mechanical property studies

Average hardness of the hot rolled plate and simulated HAZ specimen are shown in Figure 7. It can be observed that hot rolled base plate display maximum hardness of was 340 HV10. This hardness is due to deformed microstructure containing higher dislocation density. It can be inferred that the hardness values of simulated HAZ vary significantly with distance towards the base metal. While the HAZ-1 specimen displayed lowest hardness 280 HV10, the HAZ-3 specimen exhibited highest hardness of 328 HV10. Hardness of the HAZ-3 specimen was increased by 14% compared to that of the HAZ-1 specimen. This hardness variation can be related to the variation in peak temperature experienced by different HAZ leading to the differences in grain size. In addition, HAZ -1 specimen exhibited a relatively lower dislocation density compared to that of HAZ-3 specimen as seen from TEM investigations. This difference in dislocation densities is due to variation in the extent of dislocation annihilation in HAZ-1 and HAZ-3, since the specimens experienced different peak temperatures. HAZ-2 specimen showed an intermediate hardness of 294 HV10 owing to intermediate dislocation density that of HAZ-1 and HAZ-3.

Figure 8a shows the engineering stress-strain curve of hot rolled and HAZ specimens. Hot rolled specimen shows average yield strength of 945 ± 6 MPa whereas, the HAZ-1 specimen

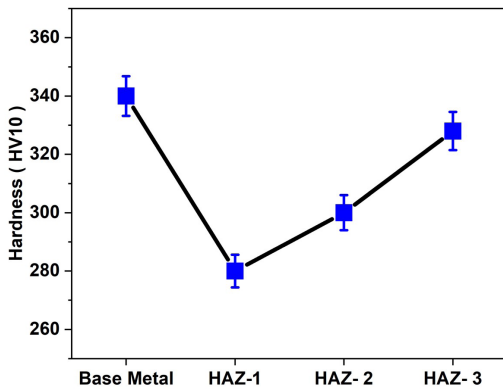


Figure 7. Comparison of Vickers hardness of hot rolled and simulated HAZ specimens with Error bars representing standard deviations.

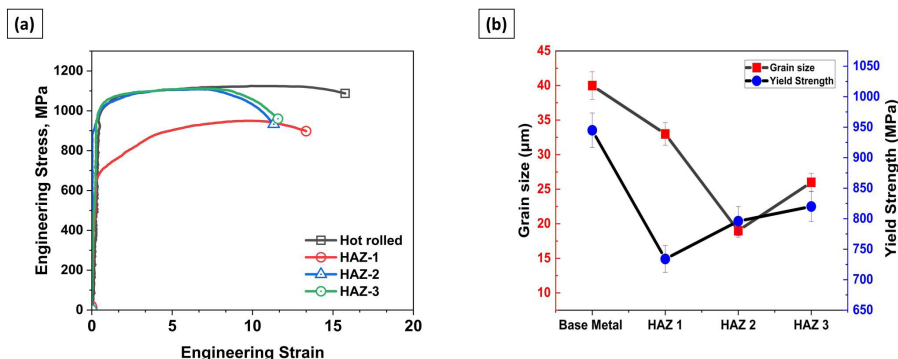


Figure 8. (a) Stress-strain curve of Hot rolled and HAZ specimens, (b) Relationship between yield strength and grain size of simulated NFNSS.

exhibited the average yield strength of 734 ± 20 MPa, which has been discussed in detail based on strengthening mechanism models. While the ultimate tensile strength of the hot rolled specimen was found to be $1127 \text{ MPa} \pm 9 \text{ MPa}$, the ultimate tensile strength of HAZ-1, HAZ-2 and HAZ-3 simulated specimen were $954 \pm 3 \text{ MPa}$, $1096 \pm 8 \text{ MPa}$, $1113 \pm 6 \text{ MPa}$ respectively. The percentage of elongation to failure of the hot rolled plate was observed to be 16%, and elongation of HAZ-1, HAZ-2 and HAZ-3 specimens were found to be 13%, 12% and 12.5% respectively. In general, the hot rolled NFNSS specimen experiences maximum yield strength in the range of (900 to 1100 MPa) and reasonable ductility in the range of 10 to 18%. It can be seen that simulated HAZ specimens experience a slight decrease in ductility compared to that of the hot rolled specimen. The difference in ductility of the HAZ specimen arises because of variations in grain sizes, formation of Cr_2N and dislocation density imposed by thermal cycles. Figure 8b shows the variation in grain size with the yield strength of the material. Yield strength of simulated HAZ samples is contributed by grain boundary strengthening and other strengthening mechanism. Thus, contribution of various strengthening on yield strength of the material is discussed.

Figure 9 micrographs shows the fracture surface morphologies of hot rolled and HAZ specimens after tensile testing. The micrographs of fracture surface in Figure 9a, exhibited dimple morphology featuring micro void formation in the hot rolled specimen, which experienced significant plastic deformation during tensile testing. Tensile test results also confirmed that hot rolled specimens exhibited a maximum ductility of 16%. Fractography analysis showed the transition from a ductile to a mixed mode of fracture surfaces in HAZ specimens because of variation in the extent of plastic deformation. HAZ-1 specimen failed by transgranular fracture owing to the nucleation and growth of cavities due to particle pull-out as indicated in Figure 9b. Both the HAZ-2 and HAZ-3 specimens exhibit a mixed-mode of fractures as shown in Figure 9c, d. As indicated in Figure 9d, some degree of particle decohesion occurred between the particle-matrix interfaces. This means that the matrix deformation was certainly limited by the presence of precipitates which tends to reduce the ductility of the HAZ-2 and HAZ-3 specimen as seen from the tensile results.

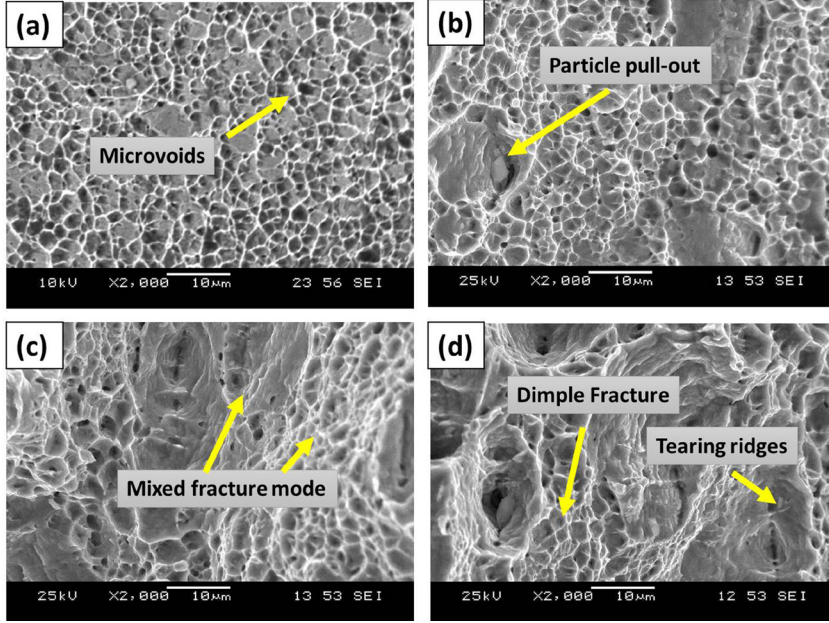


Figure 9. Fracture surface morphology of simulated NFHNSS (a) Hot rolled condition, (b) HAZ-1 specimen, (c) HAZ-2 specimen and (d) HAZ-3 specimen.

Moreover, the fracture patterned surfaces in HAZ-2 and HAZ-3 shows visible tearing ridges degrade the ductility of the specimen.

3.4. Strengthening mechanisms in NFHNSS

The theoretical yield strength of the NFHNSS can be estimated by considering four different strengthening contribution mechanisms namely solid solution strengthening (σ_{SS}), grain boundary strengthening (σ_{GB}), dislocation-assisted strengthening (σ_{DS}) and precipitation or Orowan strengthening (σ_{PS})

$$\sigma_{YS} = \sigma_{SS} + \sigma_{GB} + \sigma_{DS} + \sigma_{PS} \quad (1)$$

The solid solution strengthening of NFHNSS could be calculated using Equation 2. It is understood that alloying of interstitial elements (N, C) greatly impacts the yield strength of Fe-Mn-Cr-N austenite²⁸.

$$\sigma_{SS} = 63.5 + 496 \text{ wt. \%N} + 356.5 \text{ wt. \%C} + 20.1 \text{ wt. \%Si} + 3.7 \text{ wt. \%Cr} \quad (2)$$

The strengthening effect of grain boundaries is estimated by Hall-Petch relation²⁸

$$\sigma_{GB} = \sigma_f + K_y (d_g)^{-0.5} \quad (3)$$

Where, σ_f is the frictional stress, K_y is the Hall-Petch slope is taken as 200 MPa and 16.5³¹ and d_g is the average austenite grain size.

The Taylor equation is used to calculate dislocation strengthening is expressed as²⁶,

$$\sigma_{DS} = \alpha \mu b \rho^{1/2} \quad (4)$$

$$\rho = 2nM / Lt \quad (5)$$

Where α is a constant taken as 0.21, ρ is length of dislocation per unit volume, n is the number of intercepts with the circle, M is the magnification, L is the circumference of the circle in the micrograph and t is the foil thickness. The dislocation density were calculated using by intercept method

The resistance offered by precipitates to the passage of dislocations can be estimated using Orowan-Ashby-equation^{32,33}

$$\sigma_{PS} = \frac{0.13\mu b}{\lambda} \ln r / b \quad (6)$$

where μ the shear modulus taken as 78 GPa, b is the Burgers vector taken as 0.25 nm, r is the particle radius, $r = d_p/2$, and λ is the interparticle spacing, expressed as ,

$$\lambda = d_p \left[\left(\frac{1}{2V_p} \right)^{1/3} - 1 \right] \quad (7)$$

Where V_p is volume fraction of precipitates and particle diameter (d_p) calculated from TEM results.

Contribution of different strengthening mechanisms in base metal and simulated HAZ of NFHNSS is illustrated in Figure 10. An analysis of different strengthening mechanisms showed that solid solution strengthening appears to be the most dominant mechanism in hot rolled NFHNSS steels. Gavriljuk and Berns²⁸ discussed similar solid solution strengthening model in high nitrogen steel. The Equation 2 suggests that nitrogen plays a major role in determining the solid solution strengthening owing to the large mismatch between nitrogen and Fe atoms in steels. The next dominant strengthening mechanism is grain boundary strengthening which contributes nearly 32% to yield strength. This grain refinement may be because of thermo mechanical processing

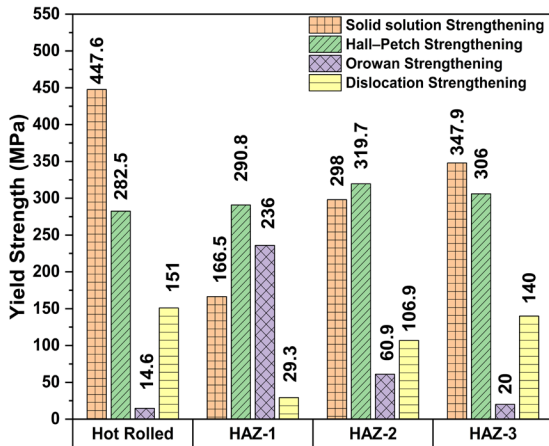


Figure 10. Contribution of various strengthening models to the yield strength of NFHNSS.

during rolling. Dislocation strengthening was found to be the next major contributor (about 16%) to the yield strength. The relative contribution of precipitation strengthening to the yield strength is 2% only. Since the volume fraction of precipitates in NFHNSS is found to be very small (less than 1%), the intensity of dislocation trapping by the particles in the Fe- Mn matrix is low and hence the precipitation hardening is not effective.

In the case of the HAZ-1 specimen, the extent of solid solution strengthening was significantly reduced from 50% to 23%. This means that most of the nitrogen atoms had reacted with chromium to form Cr_2N precipitates which drastically reduce the availability of nitrogen atoms for solid solution strengthening in the Cr-Mn matrix. This is justified since a high peak temperature of about 1052 °C experienced by the HAZ- 1 specimen, facilitated the formation of Cr_2N precipitates. Contribution of Hall-Petch or grain boundary strengthening was much higher (40%) compared to the Orowan strengthening whose contribution was about 33%. Grain refinement arises mainly because of the recrystallization during thermal cycling. While the contribution of Hall -Petch strengthening was found to be large in HAZ-2 and HAZ-3 specimens, the contribution of Orowan strengthening was higher in HAZ-1 specimen. TEM Dark-field imaging showed that fine precipitates of 0.3 volume fraction with mean diameter of 395 nm and 260 nm in HAZ-1 and HAZ-2 respectively owing to precipitation hardening. The average grain size of HAZ-2 and HAZ-3 specimens were typically in the range of 19 μm and 26 μm while it was 33 μm for HAZ-1 specimen. Such difference in grain size arising due to different peak temperature and exposure time at elevated temperatures experienced by different HAZ. Furthermore, the HAZ-3 specimen was composed of high dislocation density and bimodal grain morphology, the contribution of dislocation strengthening and Hall-Petch strengthening was found to be 17% and 37.3% respectively. Since the extent of dislocation annihilation decreases with decreasing peak temperature from HAZ-1 to HAZ-3, dislocation strengthening was higher for HAZ-3 specimen. The experimental values and theoretical predictions of yield strength are shown in Figure 11. It can be observed that the theoretical yield strength estimations correlate well with the experimental values of the NFHNSS.

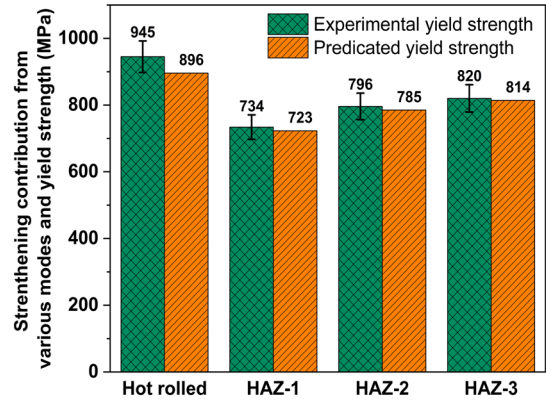


Figure 11. Predicated and Experimental yield strength of NFHNSS.

4. Conclusions

In the present work, structure-properties of simulated heat affected zone in Nickel free high- nitrogen stainless steel specimens were correlated and the major conclusions are:

1. Microstructure of hot rolled specimen showed elongated austenite grains containing a large number of annealed twins while HAZ specimens showed recrystallized austenite grains with bimodal grain morphology. Typical grain size of HAZ Specimen was found to be in the range of 33 μm to 19 μm . Such variation in grain size is due to the differences in peak temperature and cooling rate during thermal cycling.
2. Peak temperature of the different HAZ regimes chosen for simulations were found to be 1052 °C, 910 °C and 785 °C respectively. Precipitations of Cr_2N were observed in HAZ specimens with various peak temperatures. Precipitation kinetics of Cr_2N simulated in Thermo-Calc is closely in agreement with the experimental results.
3. Detailed TEM investigations showed globular Cr_2N precipitate having a hexagonal lattice orientated along [101] zone axis for HAZ-1 specimen and catenary type Cr_2N were observed in the case of HAZ-2 specimen. Only few precipitates were observed in HAZ-3 owing to thermodynamic constraints during thermal cycling.
4. Micro hardness, yield strength, the ultimate tensile strength of hot rolled specimen were found to be 340 HV10, 945 MPa and 1127 MPa respectively. In the case of HAZ specimens, micro hardness, yield strength and ultimate tensile strength were found to be in the range of 280 to 328 HV10, 734 to 820 MPa and 954 to 1113 MPa respectively.
5. Solid solution strengthening was found to be the dominant mechanism in enhancing the yield strength of the hot rolled specimen. Both the grain size strengthening and orowan strengthening appear to be the dominant strengthening mechanism for the case of HAZ specimens. This could be attributed due to recrystallization as well as the formation of precipitates during thermal cycling.

5. References

- Mohammed R, Reddy GM, Rao KS. Microstructure and pitting corrosion of shielded metal arc welded high nitrogen stainless steel. *Def Technol.* 2015;11(3):237-43.
- Woo I, Kikuchi Y. Weldability of high nitrogen stainless steel. *ISIJ Int.* 2002;42(12):1334-43.
- Lo KH, Shek CH, Lai JKL. Recent developments in stainless steels. *Mater Sci Eng Rep.* 2009;65(4-6):39-104.
- Li X, Zhang H. Analysis of microstructure and properties of welded joint of high nitrogen steel by hybrid welding. *Mater Res Express.* 2019;6(4):045602.
- Wang H, Yang DC, Liu YX, Ji CT. Research on the properties of TIG welded joints of high nitrogen nickel-free austenitic stainless steel and welding wire. *Mater Res Innov.* 2014;18(suppl 2):S2-579-S2-584.
- Liu Z, Fan C, Chen C, Ming Z, Yang C, Lin S, et al. Design and evaluation of nitrogen-rich welding wires for high nitrogen stainless steel. *J Mater Process Technol.* 2020;288:116885.
- Mohammed R, Madhusudhan Reddy G, Srinivasa Rao K. Welding of nickel free high nitrogen stainless steel: microstructure and mechanical properties. *Def Technol.* 2017;13(2):59-71.
- Mukherjee M, Pal TK. Evaluation of microstructural and mechanical properties of Fe-16Cr-1Ni-9Mn-0.12N austenitic stainless steel welded joints. *Mater Charact.* 2017;131:406-24.
- Chen TH, Yang JR. Microstructural characterization of simulated heat affected zone in a nitrogen-containing 2205 duplex stainless steel. *Mater Sci Eng A.* 2002;338(1-2):166-81.
- Wang XN, Zhao YJ, Guo PF, Qi XN, Di HS, Zhang M, et al. Effect of heat input on MA constituent and toughness of coarse grain heat-affected zone in an X100 pipeline steel. *J Mater Eng Perform.* 2019;28(3):1810-21.
- Li J, Li H, Peng W, Xiang T, Xu Z, Yang J. Effect of simulated welding thermal cycles on microstructure and mechanical properties of coarse-grain heat-affected zone of high nitrogen austenitic stainless steel. *Mater Charact.* 2019;149:206-17.
- Roncery LM, Weber S, Theisen W. Nucleation and precipitation kinetics of $M_{23}C_6$ and M_2N in an Fe-Mn-Cr-C-N austenitic matrix and their relationship with the sensitization phenomenon. *Acta Mater.* 2011;59(16):6275-86.
- Krishna Kumar K, Anburaj J, Dhanasekar R, Satishkumar T, Abuthakir J, Manikandan P, et al. Kinetics of Cr_2N precipitation and its effect on pitting corrosion of nickel-free high-nitrogen austenitic stainless steel. *J Mater Eng Perform.* 2020;29(9):6044-52.
- Lang YP, Chen HT, Weng YQ, Qu HP. Applications of ThermoCalc in research of high nitrogen austenitic stainless steels. *J Mater Eng.* 2013;3(5):16-22.
- Behjati P, Kermanpur A, Najafzadeh A, Samaei Baghbadorani H, Karjalainen LP, Jung JG, et al. Effect of nitrogen content on grain refinement and mechanical properties of a reversion-treated Ni-Free 18Cr-12Mn austenitic stainless steel. *Metall Mater Trans, A Phys Metall Mater Sci.* 2014;45(13):6317-28.
- Maier GG, Astafurova EG. A comparison of strengthening mechanisms of austenitic Fe-13Mn-1.3C steel in warm and cold high-pressure torsion. *Metals (Basel).* 2020;10(4):493.
- Farooq M. Strengthening and degradation mechanisms in austenitic stainless steels at elevated temperature [thesis]. Stockholm: KTH Royal Institute of Technology; 2013.
- Rahul MR, Phanikumar G. Correlation of microstructure with HAZ welding cycles simulated in Ti-15-3 alloy using Gleeble® 3800 and SYSWELD®. *Mater Perform Charact.* 2015;4(3):381-98.
- Liu W, Lu F, Yang R, Tang X, Cui H. Gleeble simulation of the HAZ in Inconel 617 welding. *J Mater Process Technol.* 2015;225:221-8.
- Cao R, Yang Z, Li J, Liang X, Lei W, Zhang J, et al. Effect of peak temperature on microstructure and mechanical properties of the thermally simulated welding heat-affected zones for 09MnNiDR steel. *J Mater Eng Perform.* 2020;29:7063-72.
- ASTM: American Society for Testing and Materials. ASTM E-112 standard: Standard Test Methods for Determining Average Grain Size. West Conshohocken: ASTM; 2013.
- Pettersson N, Frisk K, Fluch R. Experimental and computational study of nitride precipitation in a CrMnN austenitic stainless steel. *Mater Sci Eng A.* 2017;684:435-41.
- Rios PR, Siciliano F, Sandim H, Plaut RL, Padilha AF. Nucleation and growth during recrystallization. *Mater Res.* 2005;8(3):225-38.
- Sellars CM, Whiteman JA. Recrystallization and grain growth in hot rolling. *Met Sci.* 1979;13(3-4):187-94.
- Misra S. Austenite recrystallisation and ferrite formation in hot rolled titanium microalloyed steels [thesis]. Australia: University of Wollongong; 1986. Thesis Collection 1954-2016 [cited 2023 Feb 16]. Available from: <https://ro.uow.edu.au/theses/1607>
- Higginson RL, Sellars CM. Worked examples in quantitative metallography. Vol. 788. Boca Raton: CRC Press; 2003.
- Li Jy, Liu Hn, Huang Pw. Effects of pre-precipitation of Cr_2N on microstructures and properties of high nitrogen stainless steel. *J Cent South Univ Technol.* 2012;19(5):1189-95.
- Gavriljuk VG, Berns H. High nitrogen steels: structure, properties, manufacture, applications. USA: Springer Science & Business Media; 1999. 394 p.
- Lee TH, Oh CS, Han HN, Lee CG, Kim SJ, Takaki S. On the crystal structure of Cr_2N precipitates in high-nitrogen austenitic stainless steel. *Acta Crystallogr B.* 2005;61(2):137-44.
- Zhang J, Xin W, Luo G, Wang R, Meng Q, Xian S. Effect of welding heat input on microstructural evolution, precipitation behavior and resultant properties of the simulated CGHAZ in high-N V-alloyed steel. *Mater Charact.* 2020;162:110201.
- Zhao W, Wang W, Chen S, Qu J. Effect of simulated welding thermal cycle on microstructure and mechanical properties of X90 pipeline steel. *Mater Sci Eng A.* 2011;528(24):7417-22.
- Zhang Z, Chen DL. Consideration of Orowan strengthening effect in particulate-reinforced metal matrix nanocomposites: A model for predicting their yield strength. *Scr Mater.* 2006;54(7):1321-6.
- Machavallavan N, Singh H, Surappa M. Processing, microstructural evolution and strength properties of in-situ magnesium matrix composites containing nano-sized polymer derived SiCNO particles. *Mater Sci Eng A.* 2017;685:429-38.